Retrieval of Atmospheric Water Vapor and Temperature Profiles over Antarctica from Satellite Microwave Observations Using an Iterative Approach

Zhimeng Zhang[1], Shannon Brown[2], Andreas Colliander[2]

[1]California Institute of Technology, Pasadena, CA, USA

[2]Jet Propulsion Laboratory, California Institute of Technology, Pasadena, CA, USA

Correspondence to: Zhimeng Zhang (zhimeng@caltech.edu)

Abstract.

Retrieving atmospheric water vapor and temperature profiles over land using microwave radiometry is challenging due to uncertainties in estimating surface emissions. To address this, we developed an approach that couples the atmospheric retrieval algorithm with the surface emission estimation in an iterative loop. Using sounding channels from Ka- to G- band on the Advanced Technology Microwave Sounder (ATMS), we retrieved temperature and humidity profiles across the Antarctic region throughout the year 2016. The atmospheric profiles are updated in each iteration and used in the following step to refine the surface emissivity. This process continues until the atmospheric solution converges. The main innovation is the integration of surface and atmospheric retrievals, which improves overall accuracy. We validated our results against in-situ radiosonde data. The algorithm accurately retrieved temperature profiles, along with surface emissivity across 23–165 GHz, and successfully detected ice sheet meltings. While it captured water vapor variability, accurate absolute humidity values still require an independent surface emissivity retrieval using additional observations.

1   Introduction

The Greenland and Antarctica ice sheets are major contributors to global sea level rise due to increasing ice melt. [Rignot et al. 2011]. This highlights the need to monitor and understand the mechanisms driving the accelerated melt events [Noble et al. 2020]. Effectively monitoring and analyzing the ice sheets require a detailed understanding of the atmospheric conditions that influence these regions [Le clec'h et al. 2019], which is also essential for predicting the future evolution of ice masses [Le clec'h et al. 2019]. Current atmospheric temperature and humidity retrievals in the microwave spectral range face challenges, primarily due to uncertainties in estimating surface emission. These challenges are amplified over polar ice sheets, where the atmosphere is typically dry, the surface emissivity changes rapidly during melt seasons, and the background emission is relatively high [Miao et al., 2001]. Traditional retrievals are limited by the absence of direct surface emissivity measurements and uncertainties in modeling background emission. To overcome these issues, we implement an iterative strategy that couples atmospheric retrieval with surface emission estimation. This approach enhances the accuracy of retrieved atmospheric temperature and humidity profiles, supporting improved understanding of the processes that drive melt in the Greenland and Antarctic ice sheets.

34

The Advanced Technology Microwave Sounder (ATMS), on board polar-orbiting satellites, is designed to perform atmospheric temperature and humidity sounding through oxygen and water vapor absorption bands [Goldberg et al. 2006, Muth et al. 2005]. We applied our iterative retrieval algorithm to ATMS data across Antarctica during 2016. This year was selected due to the significant melt anomaly over Ross Ice Shelf during 2016 austral summer (e.g., Nicolas et al., 2017; Mousavi et al., 2022; de Roda Husman et al., 2024; Hansen et al., 2024), which provided ideal conditions to assess the impact of varying surface emissivity on atmospheric retrievals. This analysis enabled us to evaluate the performance and limitations of the iterative approach.

2   Observations

2.1   Observation Data - ATMS data

The satellite carrying ATMS follows a sun-synchronous polar orbit, completing about 14 orbits per day and enabling frequent revisit opportunities, especially at high latitudes. Over the Antarctic region, this results in 4 to 10 ATMS overpasses per day for any fixed location, with variations due to swath width (~2,500 km), scan angle geometry, and Earth rotation. ATMS has 22 channels to receive and measure radiation from different layers of the atmosphere, obtaining global data on tropospheric humidity and temperature at either quasi-vertical or quasi-horizontal polarization. Table 1 summarizes the radiometric characteristics of the ATMS channels, while Figure 1 shows their spectral positions relative to atmospheric opacity from oxygen and water vapor absorption. ATMS channels cover the oxygen band (50–58GHz), the two water vapor lines at 22 GHz and 183 GHz, and several window channels (see Fig. 1). The temperature information of the atmosphere is obtained from Channels 3-15. Channels 18-22 are centered at the 183.31 GHz water vapor line but with a successively narrower bandwidth from ±7GHz to ±1GHz, giving humidity information on successively higher troposphere.

Figure 1 shows the zenith opacity of a typical polar dry atmosphere for the ATMS frequency range. The opacity is dominantly caused by water vapor and oxygen in the atmosphere. The contribution of nitrogen, orders of magnitude smaller and without any spectral line at this frequency range, can be neglected. The total opacity is computed by integrating the opacity per unit length from the top of the atmosphere toward the surface [Meeks and Lilley 1963]. Channels 1, 2, 16, and 17 are located at transparent window regions, where the opacity is low. Jacobians of temperature and water vapor channels typically peak near the maximum of the weighting function, which often corresponds approximately to the atmospheric level where the optical depth is near unity [Petty 2004]. For the window channels, the overall opacity is much less than one. These channels can see through the atmosphere and are sensitive to Earth's surface emission; therefore, they can be used for deriving surface emissivity. However, at oxygen (58 GHz) and water vapor (183 GHz) absorption bands, the observed brightness temperature is not very sensitive to the surface emission. The surface emissivity at these frequencies will be derived using the adjacent channels that have relatively low opacity: CH3 (50.3 GHz) will be used to derive the emissivity in the range of 50.3-57.29 GHz (CH3 to CH15) at QH polarization; CH18 (183.31$\pm$7 GHz) for the emissivity near 183.31 GHz (CH18 to CH22) at QH polarization. In all, we derive surface emissivity for the window channels 1 (23.8 GHz), 2 (31.4 GHz), 3 (50.3 GHz), 16 (88.2 GHz), 17 (165.5 GHz), and 18 (183.31$\pm$7GHz), and assume linear emissivity variation between these frequencies.

71
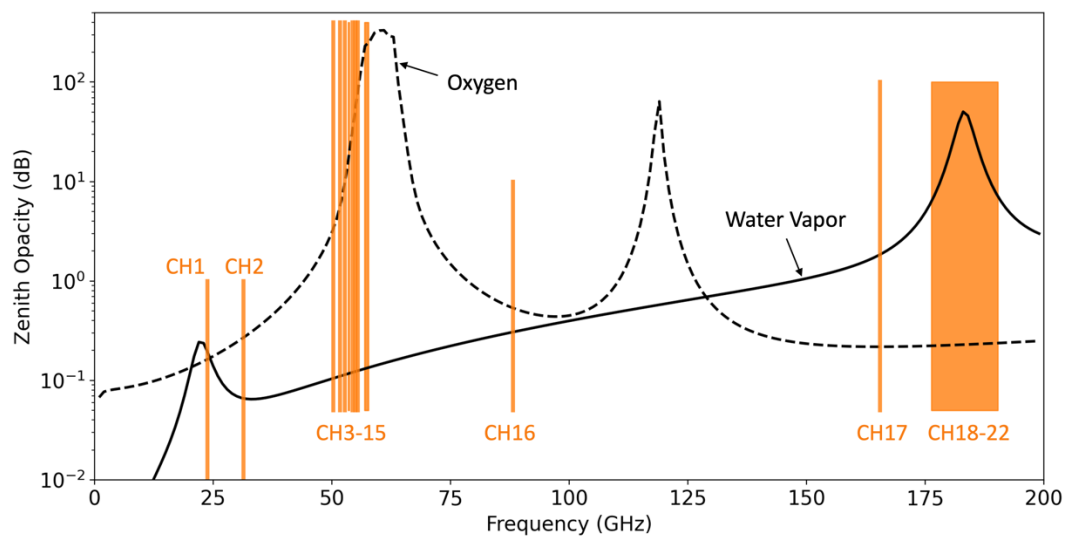
72   **Figure 1** Spectra positions of 22 ATMS channels, on top of zenith opacity from oxygen and water vapor.

73

74 **Table 1** Key characteristics of the 22 ATMS channels.

Channel	Central frequency [GHz]	$NE\Delta T$ [K]	Beam Width	Ground Res. (Nadir)	Polarization
1	23.8	0.7	5.2°	75km	QV
2	31.4	0.8	5.2°	75km	QV
3	50.3	0.9	2.2°	32km	QH
4	51.76	0.7	2.2°	32km	QH
5	52.8	0.7	2.2°	32km	QH
6	53.596 ± 0.115	0.7	2.2°	32km	QH
7	54.4	0.7	2.2°	32km	QH
8	54.94	0.7	2.2°	32km	QH
9	55.5	0.7	2.2°	32km	QH
10	57.290344	0.75	2.2°	32km	QH
11	57.290344 ± 0.217	1.2	2.2°	32km	QH
12	57.290344 ± 0.3222 ± 0.048	1.2	2.2°	32km	QH
13	57.290344 ± 0.3222 ± 0.022	1.5	2.2°	32km	QH
14	57.290344 ± 0.3222 ± 0.010	2.4	2.2°	32km	QH
15	57.290344 ± 0.3222 ± 0.0045	3.6	2.2°	32km	QH
16	88.2	0.5	2.2°	32km	QV
17	165.5	0.6	1.1°	16km	QH
18	183.31 ± 7.0	0.8	1.1°	16km	QH
19	183.31 ± 4.5	0.8	1.1°	16km	QH
20	183.31 ± 3.0	0.8	1.1°	16km	QH
21	183.31 ± 1.8	0.8	1.1°	16km	QH
22	183.31 ± 1.0	0.9	1.1°	16km	QH

75

76 The beam width of ATMS varies with frequency: 1.1° for channels in the 160-183 GHz range, 2.2° for the 50-60 GHz

77 and 80 GHz channels, and 5.2° for the 23.8 GHz and 31.4 GHz channels [Kim et al. 2014, 2020]. Both SNPP (Suomi

78 National Polar-orbiting Partnership) and the NOAA-20 (National Oceanic and Atmospheric Administration 20, also

79 known as Joint Polar Satellite System 1, JPSS-1) satellites orbit at an altitude of approximately 830 km. This results

80 in instantaneous spatial resolutions on the ground at nadir about 16 km, 32 km, or 75 km, depending on the channels.

81 Due to the cross-track scanning approach, the instrument provides observations at a wide range of incidence (off-nadir)

82 angles. To ensure accuracy, we include only observations with an incidence angle less than 60°, as the instrument

83 footprint increases approximately with $1/(\cos^2\theta)$. For each fixed reference location, we use only those ATMS

84 observations whose beam boresight lies within 22.24 km (corresponding to 0.2° angular separation), ensuring spatial

85 relevance. The ATMS data used in this work were obtained from the Comprehensive Large Array-data Stewardship

86 System (CLASS) of NOAA.

87

88   To better understand the vertical sensitivity of each ATMS channel to atmospheric temperature and water vapor, we

89   examine the Jacobians, which describe how changes in these variables influence observed brightness temperature.

90   Figure 2 shows the temperature (upper right) and water vapor (lower right) Jacobians at all 22 ATMS channels for

91   December (austral summer) atmospheres, representative of Antarctica conditions. The Jacobians are calculated by

92   increasing the water vapor and temperature at each vertical layer to the orange dashed line, using the same 73-layer

93   vertical grid as MERRA profiles (see Section 2.2), ranging from two meters above the surface to over 70 km in altitude.

94   Therefore, a positive value implies that adding water vapor or increasing temperature will increase the radiance

95   observed by the instrument and vice versa. The Jacobian shows the sensitive altitudes of each channel. Near the oxygen

96   absorption band, CH3 to CH15 are sensitive to successively higher altitudes, up to ~60 km above the sea level.

97   Channels 18–22 are located near the water vapor line at 183.31 GHz. The atmospheric opacity for these channels

98   differs significantly, making these channels sensitive to different layers of the atmosphere. The bandwidth of these

99   channels decreases with the channel number, with Channel 22 being the narrowest and Channel 18 being the broadest.

100   The water vapor Jacobians for Channels 18–22 indicate sensitivity to distinct atmosphere layers extending up to

101   several kilometers above the surface. Above approximately 10 km, the atmospheric water vapor content is so low that

102   typical perturbations fall below the detection threshold of ATMS. The Jacobians shown are from the nadir view (0°

103   incidence angle). Jacobians corresponding to off-nadir angles peak at slightly higher altitudes due to the longer

104   atmospheric path length traversed by the radiation.

105
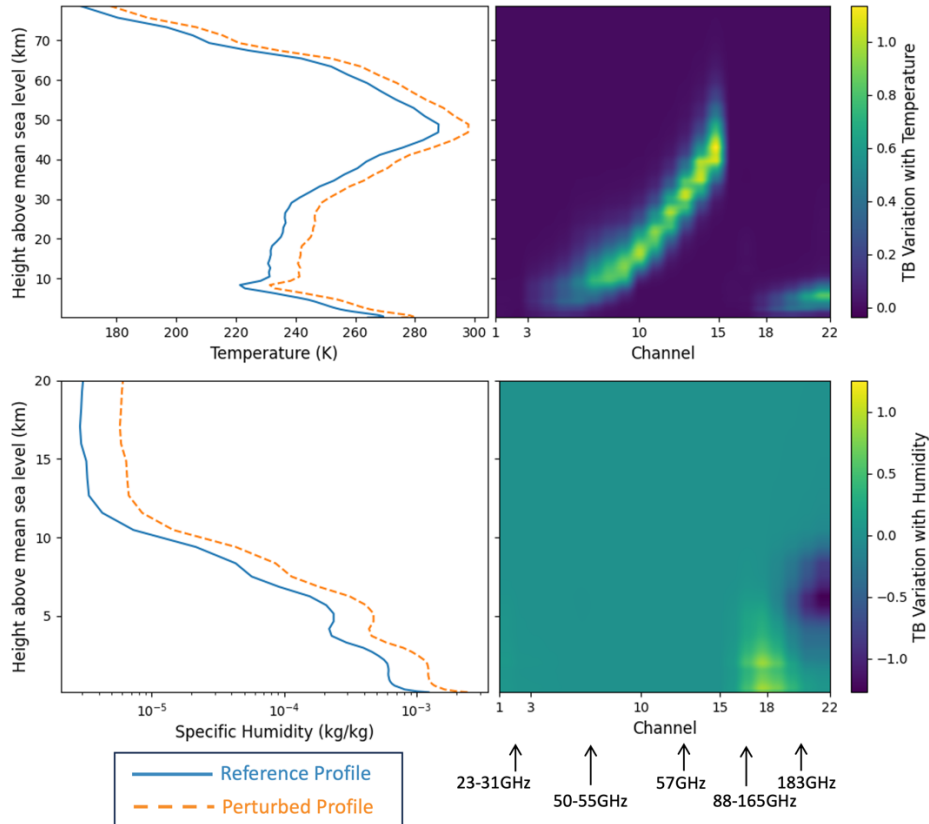
106

Figure 2 Typical Antarctica atmospheres for summer (December) weathers at WAIS DIVIDE (79.5ºS, 112ºW). The plots show the temperature profile (upper left) and the specific humidity profile (lower left), the temperature Jacobian (upper right), and the water vapor Jacobian (lower right) for all 22 ATMS Channels. The Jacobians are based on nadir view (0º incidence angle).

2.2   The Prior – MERRA-2

Using ATMS microwave thermal emission measurements, we applied Optimal Estimation (OE) to retrieve the atmospheric temperature and humidity profiles. OE, as outlined by Maahn et al. (2020), is a widely used physical retrieval method that incorporates measurements, prior information, and their uncertainties. Based on Bayes' theorem, OE estimates the most probable atmospheric state. Prior information plays a critical role in the retrieval process. We use the Modern-Era Retrospective analysis for Research and Applications, version 2 (MERRA-2) as the prior for temperature and water vapor profiles. We use the "tavg3_3d_asm_Nv" dataset, which offers three-hourly averaged atmospheric profiles across 72 hybrid sigma-pressure levels [Rienecker et al. 2008], with a spatial resolution of 0.625º longitude by 0.5º latitude. For ice and liquid water cloud distributions, we used the MERRA-2 3D cloud fields, which provide vertically and horizontally resolved profiles of cloud water and ice content. To account for surface characteristics such as skin temperature, temperature/humidity/wind speed at two meters, and surface pressure, we integrated MERRA-2 single-level diagnostics data labeled as "tavg1_2d_slv_Nx". By merging the three-dimensional assimilated meteorological data with the single-level diagnostics data, our analysis extends across 73 vertical layers starting from two meters above the surface and extending beyond 70 kilometers into the atmosphere. The vertical grid is close to equidistant in the logarithm of the pressure and approximately equidistant in altitude.

To illustrate the structure and seasonal variability of the a priori profiles used in the retrievals, Figure 3 presents the seasonal mean temperature and specific humidity profiles from MERRA-2 at three representative Antarctic sites: McMurdo Station, the South Pole, and the Antarctic Peninsula. These locations span different climate regimes, and the profiles exhibit clear seasonal contrasts—especially the colder, drier winter atmosphere and the distinctive temperature inversions near the tropopause. This spatial and temporal variability highlights the importance of location- and season-specific a priori knowledge in OE retrievals. It is also important to note that the MERRA-2 priors are provided with respect to height above mean sea level, and the surface elevation differences among the selected sites (e.g., higher elevation at the South Pole vs. coastal McMurdo) are preserved in the a priori structure. This ensures that retrievals remain physically consistent with the local topography and atmospheric structure. In addition to the mean state profiles, the OE algorithm also incorporates the a priori error covariance matrix, which encodes the expected variability and vertical correlation of atmospheric parameters. It plays a critical role in weighting the influence of the prior relative to the measurements and governs the vertical smoothing and retrieval precision.
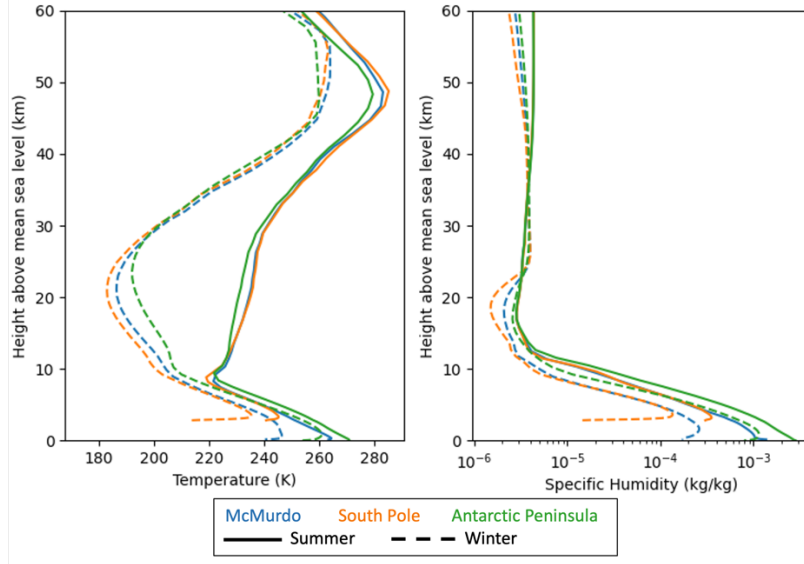
Figure 3 Seasonal average profiles of temperature (left) and specific humidity (right) from MERRA-2 for three representative Antarctic locations: McMurdo Station, the South Pole, and the Antarctic Peninsula. Solid lines represent summer; dashed lines represent winter. These profiles are used as a priori inputs in the retrieval algorithm and illustrate regional and seasonal variability in atmospheric conditions.

2.3   In Situ and Ground-Based Remote Sensing Observations

Across Antarctica, a network of radiosonde stations provides in situ measurements of atmospheric profiles. These stations contribute to the Integrated Global Radiosonde Archive (IGRA), which provides valuable long-term in situ measurements, though often at limited temporal resolution depending on station operations [Durre et al. 2006]. However, efforts such as the Atmospheric Radiation Measurement (ARM) West Antarctic Radiation Experiment (AWARE) have enhanced observational capabilities by delivering high-temporal-resolution radiosonde data at key locations, including the West Antarctica Ice Sheet (WAIS) and McMurdo Station [Lubin et al. 2017]. AWARE employed ground-based remote sensing instruments, such as microwave radiometers, Atmospheric Emitted Radiance Interferometers (AERIs), and cloud radar systems, to derive continuous atmospheric profiles of temperature and humidity. To approximate higher temporal resolution, AWARE introduced an interpolated atmospheric profile product. While AWARE did include multiple radiosonde launches per day, the 1-minute time-resolution profiles were not direct radiosonde observations but were interpolated between sonde launches and adjusted using integrated water vapor values derived from microwave radiometer observations. These ground-based retrievals assume horizontal homogeneity and are subject to radiative transfer model assumptions. They typically offer high temporal resolution (1-minute) but at lower vertical resolution (often on the order of hundreds of meters) compared to radiosonde profiles (with vertical resolution of 20–200 meters). These profiles capture fine-scale temperature and humidity structures that are crucial for validating satellite and model retrievals.

In our study, we evaluated the performance of the iterative retrieval algorithm using data from 5 radiosonde stations across Antarctica during 2016. This assessment allowed us to test the algorithm under a range of atmospheric conditions, geographical settings, and ice sheet melting scenarios. Retrieval results were compared against radiosonde-derived temperature and humidity profiles, serving as a benchmark for assessing accuracy. Importantly, radiosonde profiles were used solely for validation and not as climatological priors in the retrieval process, as our goal is to enable retrievals across all of Antarctica, including areas without radiosonde coverage. The validation results provided valuable insights into the strengths and limitations of our method, and informed refinements to improve its accuracy and reliability for atmospheric and cryospheric studies.

Table 2 In-situ and ground-based remote sensing observations stations showed in this study.

IGRA (Daily)				177
SYOWA	69.0053^o S	39.5811^o E	2016 Jan.1 – March.31	Fig. S2
DAVIS	68.5744^o S	77.9672^o E	2016 Jan.1 – Feb.29 2016 Nov.15 – Dec.31	Fig. S1
MARIO ZUCHELLI STATION	74.6958^o S	164.0922^o E	2016 Jan.1 – Feb.29	Fig. S3
AWARE Campaign (1-Minute Interval)				
McMurdo Station	77.85^o S	166.66^o E	2016 Jan.1 – Dec.31	Fig. 9
WAIS Divide	79.468^o S	112.086^o W	2016 Jan.1 – Jan.17	Fig. 10

3   Iterative Retrieval Algorithm

3.1 Iterative Process

We developed a channel-selective iterative approach to retrieve surface emissivity along with the atmospheric temperature and humidity profiles, as illustrated in Figure 4. The procedure begins with an initial estimation of surface emissivity, which is then used to derive temperature and humidity profiles. Next, these profiles are utilized to refine the surface emissivity in a continuous loop until the update in emissivity reaches a margin of 0.01. Typically, the results converge within six iterations. The final discrepancy between observed and modeled brightness temperatures (the residual) is compared against the noise equivalent delta temperature to assess the accuracy. The noise equivalent delta temperature (NEΔT) represents the level of instrument noise inherent in brightness temperature measurements. For a total power radiometer like ATMS, NEΔT is influenced by several system-level factors, including the system noise temperature (which incorporates atmospheric and instrumental contributions), the radiometer's bandwidth, the integration time, and fluctuations in instrument gain. Any residual falling within 1.5 times the noise equivalent delta temperature is considered a valid match. The outcome of the retrieval includes the profiles of temperature and humidity as well as the surface emissivity for all frequency channels (23GHz to 183GHz). We initialize emissivity $\varepsilon_0 = 0.8$

194   across all frequencies, based on the average AMSU-A surface emissivity values previously reported for the Antarctic

195   region [Spencer and William 1999]. In Figure 5, we present a histogram of surface emissivity values archived in

196   AMSU-A data at 23 GHz, 31 GHz, and 50 GHz across the Antarctic region during 2016, showing a median value near

197   0.8. These emissivity values were calculated directly from satellite observations under clear-sky conditions, following

198   the methodology of Ferraro et al. (2018).

199

200
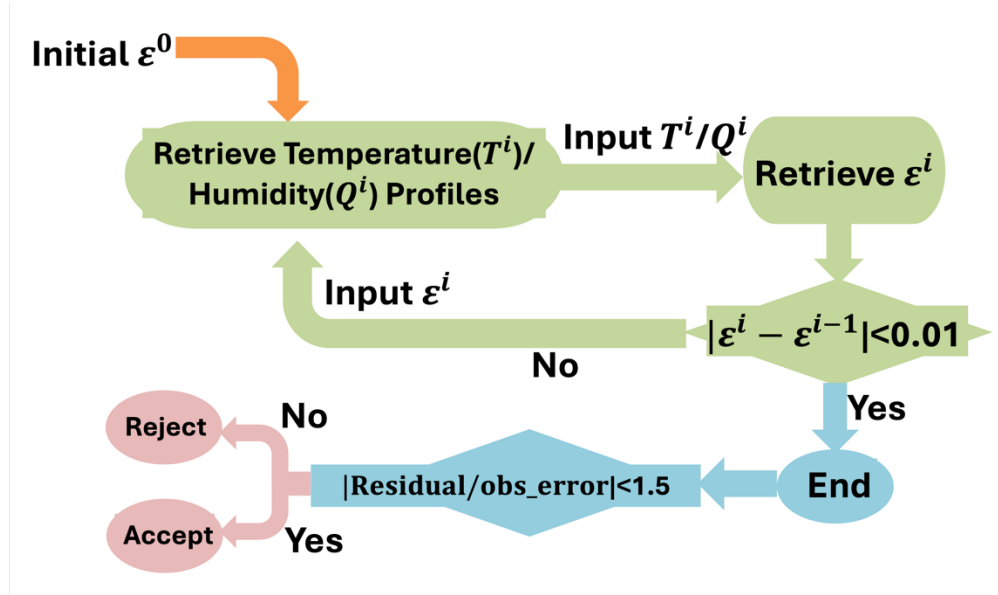
201   **Figure 4** Flow diagram of the iterative retrieval process. The process starts with an initial guess of surface emissivity

202   ε^0 to retrieve temperature T^i and humidity profiles Q^i, which are then utilized to adjust the surface emissivity ε^i for

203   subsequent iterations. Residuals are defined as the difference between observed and modeled brightness temperature

204   and assessed against the observation noise equivalent delta temperature. Any residual falling within 1.5 times the noise

205   equivalent delta temperature is considered a valid match. The final outcomes are the temperature and humidity profiles

206   alongside the surface emissivity.

207

208
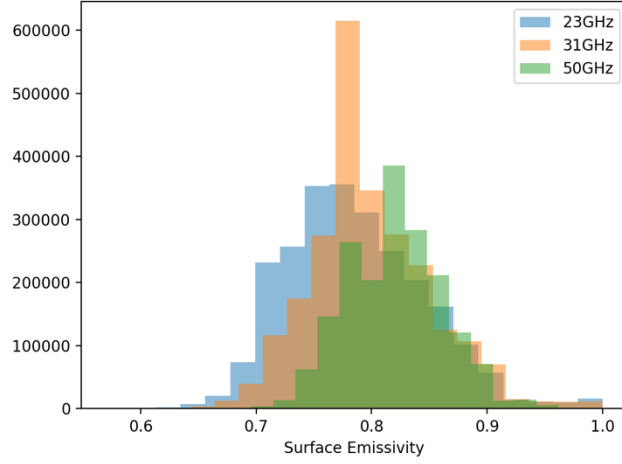
209   **Figure 5** Histogram of AMSU-A surface emissivity values at 23 GHz, 31 GHz, and 50 GHz over the Antarctic region

210   during 2016. These values are obtained from the AMSU-A emissivity data archive. The median emissivity across

211   these frequencies is near 0.8, which serves as the initial value (ε_0) in our iterative retrieval process.

212

213   **3.2   Forward Model - Radiative Transfer Model**

214

215   RTTOV (Radiative Transfer for TOVS[1]) is a fast radiative transfer code widely used in atmospheric remote sensing

216   research [Saunders et al. 2018]. The model incorporates detailed representations of atmospheric properties, including

217   temperature, humidity, pressure, and optionally, trace gases, aerosols, and hydrometeors, together with surface

218   parameters and viewing geometry, allowing for accurate simulations of radiative transfer processes in diverse

219   atmospheric conditions. We incorporate a Python interface written for RTTOV v11.3. The model was not only used

220   to calculate radiances but also to calculate the associated Jacobians. The profile is assumed to be linear between the

221   vertical grid points. The grid used is close to equidistant in the logarithm of the pressure; hence, it is approximately

222   equidistant in altitude. RTTOV computes the top-of-atmosphere radiances from both atmospheric and surface

223   emission in each of the sensor channels. The radiance can be represented as:

224   $$L(\nu) = \int_{\tau_s}^{1} B(\nu, T) d\tau + [1 - \varepsilon_s(\nu)] \cdot \tau_s^2(\nu) \cdot \int_{\tau_s}^{1} \frac{B(\nu, T)}{\tau^2} d\tau + \varepsilon_s(\nu) \cdot \tau_s(\nu) \cdot B(\nu, T_s) , \qquad \dots[1]$$

225   where L is the radiance at frequency ν; $B(\nu, T)$ is Planck's law; τ is the transmittance from the top of the atmosphere

226   to depth τ, and τ_s is the transmittance from the top of the atmosphere to the surface, both of which depend mostly on

227   oxygen and water vapor absorption; ε_s is the surface emissivity, while $1 - \varepsilon_s$ is the respective surface reflectivity, and

228   T_s is the surface skin temperature. The three terms on the right-hand side correspond to the upwelling atmospheric

229   emission, the downwelling atmospheric emission reflected by the surface, and the surface emission respectively.

---

[1] **TOVS:** Television InfraRed Observation Satellite (TIROS) Operational Vertical Sounder, a suite of three instruments that measure upwelling radiation from the atmosphere from which surface properties, clouds, and the vertical structure of the atmosphere can be determined.

230

3.3   Retrieved Profiles

232

We utilized our iterative retrieval method, as described in Section 3.1, on the ATMS data collected over the Antarctica region during 2016. Figure 6 presents an example of the retrieval evolution over six iterations, including temperature profiles (top left), specific humidity profiles (top right), and frequency-dependent surface emissivity (bottom left). The bottom right panel shows the residual (the difference between observation and model) divided by the observation noise. As discussed in Section 3.1, if the residuals for all frequencies/channels are under 1.5 times of the noise, the model is considered a valid match. Following six iterations, we observe convergence in the iterative process. Fig.6 shows temperature profiles up to 16 km above sea level and specific humidity profiles up to 10 km, corresponding to the altitude range covered by available radiosonde data. In the upper two panels, the purple curves display the radiosonde *in situ* measurements, used to validate the iterative retrieval algorithm. The radiosonde measurements reveal fine-scale temperature and humidity structures–with vertical resolution ranging from 20 m to a few hundred meters– that the microwave radiometer-based algorithms cannot resolve. Despite these fine features, the temperature profile obtained through iterations matches the radiosonde measurements. The specific humidity below 6 km also shows good agreement with the measurements. However, the retrieval method becomes less sensitive above 6 km, primarily due to humidity levels that are orders of magnitude lower at higher altitudes.

247

As shown in Eqn.1, when atmospheric profiles are known, the observed brightness temperature from the top of the atmosphere can be expressed as a linear function of the surface emissivity. By combining radiosonde-measured atmospheric profiles with ATMS brightness temperatures, we compute the surface emissivity at ATMS frequencies, referred to as the radiosonde reference surface emissivity (the black dotted line, the lower left panel in Figure 6). Our iteratively retrieved surface emissivity (red curve) is in good agreement with these radiosonde reference values. However, at 183 GHz - the water vapor absorption band - surface emission is tightly coupled with near-surface humidity, making accurate emissivity retrieval more difficult. As a result, the iterative method may yield less reliable results at this frequency (see Section 4.1). Using the reference surface emissivity, the black dotted lines in the upper panels of Fig. 6 represent the best-fit atmospheric profiles achievable with ATMS's 22 channels, serving as a benchmark for evaluating our iterative retrieval approach. The comparison between the radiosonde reference profile and the iterative retrieved profile in the upper panels indicated a high level of consistency.
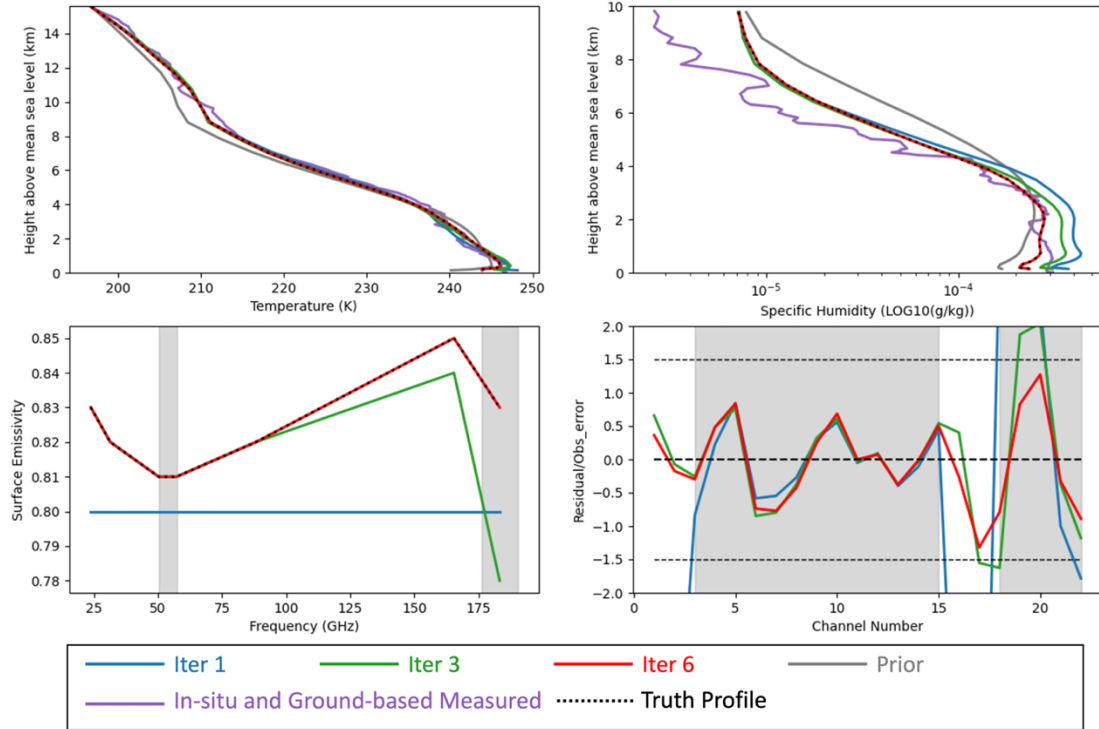
Figure 6 Retrieved temperature profiles (top left), specific humidity profiles (top right), and frequency-dependent surface emissivity (lower left) over six iterations (for clarity, only iterations 1, 3, and 6 are displayed). The lower right panel shows the residual divided by the observation noise (the model's fit is considered good when the absolute residuals at all frequencies are less than 1.5 times of the noise, indicated by the dashed lines). The iteration process converges within six iterations. The gray curve shows the prior for the temperature and humidity profiles. In the bottom two figures, the oxygen and water vapor absorption frequency bands/channels are shaded in gray. In the upper two panels, the purple curve shows the radiosonde *in situ* measurements. The black dotted line shows the reference profiles retrieved using the radiosonde reference emissivity. This demonstrated example is a particularly good fit where the retrieved surface emissivity closely matches ARM-derived values; not all cases show this level of agreement.

4   Validation and Discussion

We assess the performance of our iterative retrieval method by comparing the retrieved atmospheric profiles with radiosonde measurements. This comparison demonstrates both the capability and limitations of our approach in capturing seasonal variations and surface-atmosphere interactions across Antarctica.

4.1 Mid-January 2016 Melting Event Near the Ross Ice Shelf

In this section, we examine the atmospheric and surface conditions during the mid-January 2016 melting event by analyzing retrieval results at three key Antarctic sites—McMurdo Station, WAIS Divide, and Ross Ice Shelf—over

279 the same time period, each of which shows corresponding variations in atmospheric profiles, surface emissivity, or

280 both during the melt.

281

282 **McMurdo Station**

283

284 The McMurdo Radiosonde Station is located on Ross Island at coordinates 77.85ºS, 166.66ºE. In 2016, radiosonde

285 observations were obtained with high temporal resolution at this station. Figure 7 presents a histogram of the

286 differences between atmospheric profiles retrieved by our iterative algorithm and the radiosonde reference profiles as

287 described in Section 3.3. The upper panels depicts the temperature difference below 70 km height, while the lower

288 panels shows the specific humidity difference below 10 km height, spanning the entire year of 2016. The left panels

289 show the median value and the 68% confidence intervals (one standard deviation). The accuracy of the temperature

290 profile retrieval was high, with a standard deviation of 0.5K. However, while most humidity variations were detectable

291 (to be further discussed in the next paragraph), the absolute value was not precise compared to the measurement, with

292 a standard deviation of approximately 25%. The humidity was strongly linked to the surface emissivity at 183 GHz.

293 In addition to the iteratively retrieved profiles, we also include histograms of deviations for the MERRA-2 archived

294 profiles as a baseline. The results indicate that the iterative retrieval approach improves accuracy in both temperature

295 and humidity, yielding distributions more closely aligned with radiosonde-derived observations. Fig. 8 shows the

296 histogram displaying the difference between the surface emissivity retrieved iteratively and the radiosonde reference

297 value. The surface emissivity retrieved iteratively is highly accurate within a range of ±0.01 for window channels like

298 23.8 GHz, 31.4 GHz, and 88.2 GHz. In the oxygen absorption band between 50 and 58 GHz, most of the retrieved

299 surface emissivity values fall within ±0.02 of the radiosonde reference value, aligned with the fact that retrieved

300 temperatures have a one-sigma difference within ±0.5K from the actual value. The channels above 165 GHz are

301 affected by water vapor absorption. At 165 GHz, the emissivity retrieval shows a standard deviation of 0.03, while at

302 183 GHz, the standard deviation increases to ~0.1. These discrepancies are too substantial to permit accurate retrieval

303 of the humidity profile. An independent estimate of the ice sheet surface emissivity is required to separate the effects

304 of ice sheet emissions and atmospheric humidity.
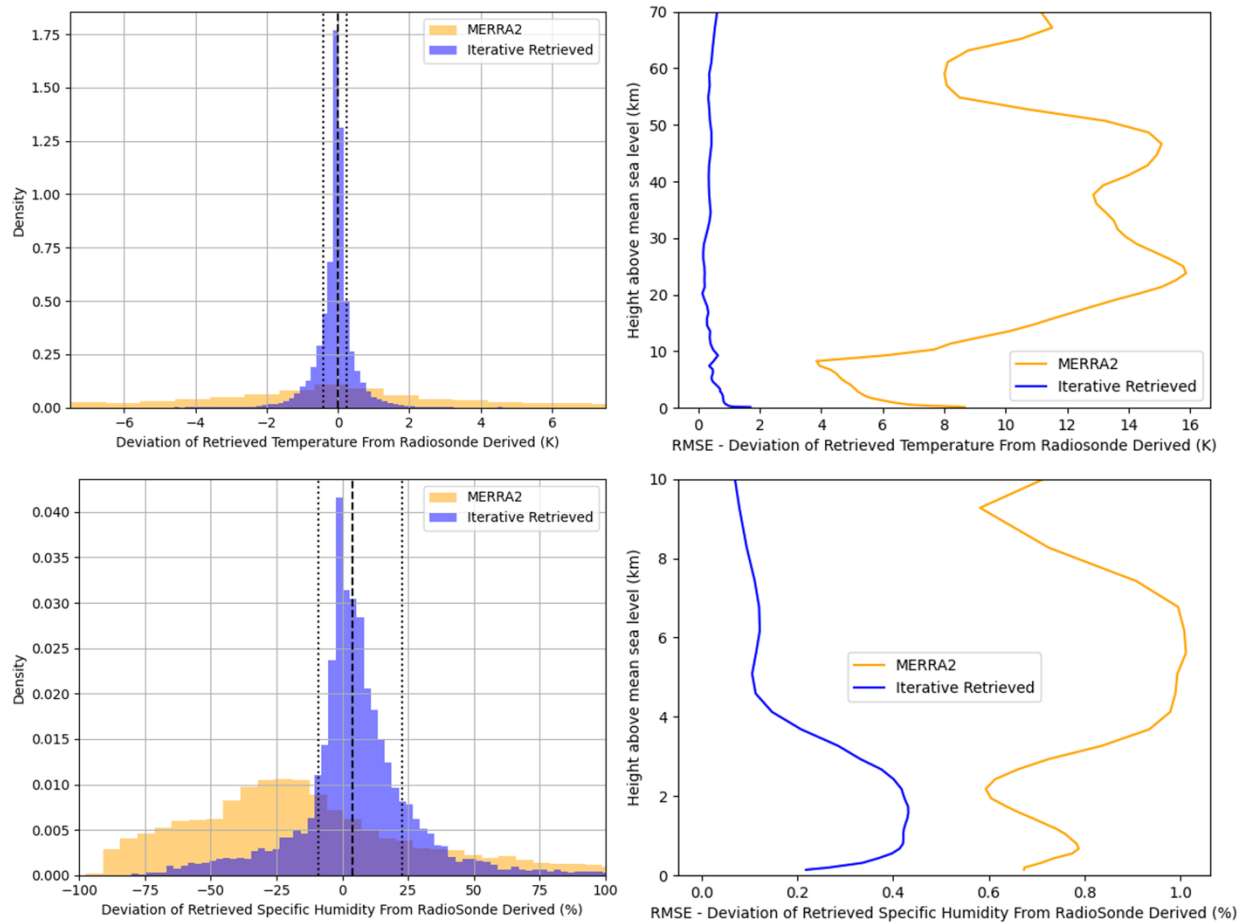
Figure 7 Histogram of the differences between atmospheric profiles retrieved by our iterative algorithm and the radiosonde reference profiles. The upper panels shows temperature differences below 70 km (in K), and the lower panels shows specific humidity differences below 10 km, expressed as a percentage relative to the reference profiles. We use percentage differences for specific humidity to account for its strong vertical gradient, which spans approximately two orders of magnitude; this approach avoids biasing the evaluation toward near-surface values. In the left column, dashed black lines represent the median and the 68% confidence interval (one standard deviation) in each panel. Same histograms for the MERRA-2 profiles are included as a baseline, demonstrating that the iterative retrieval method improves agreement with observations by reducing deviations in both temperature and humidity. The right column show the root mean square error (RMSE) with respect to altitude.
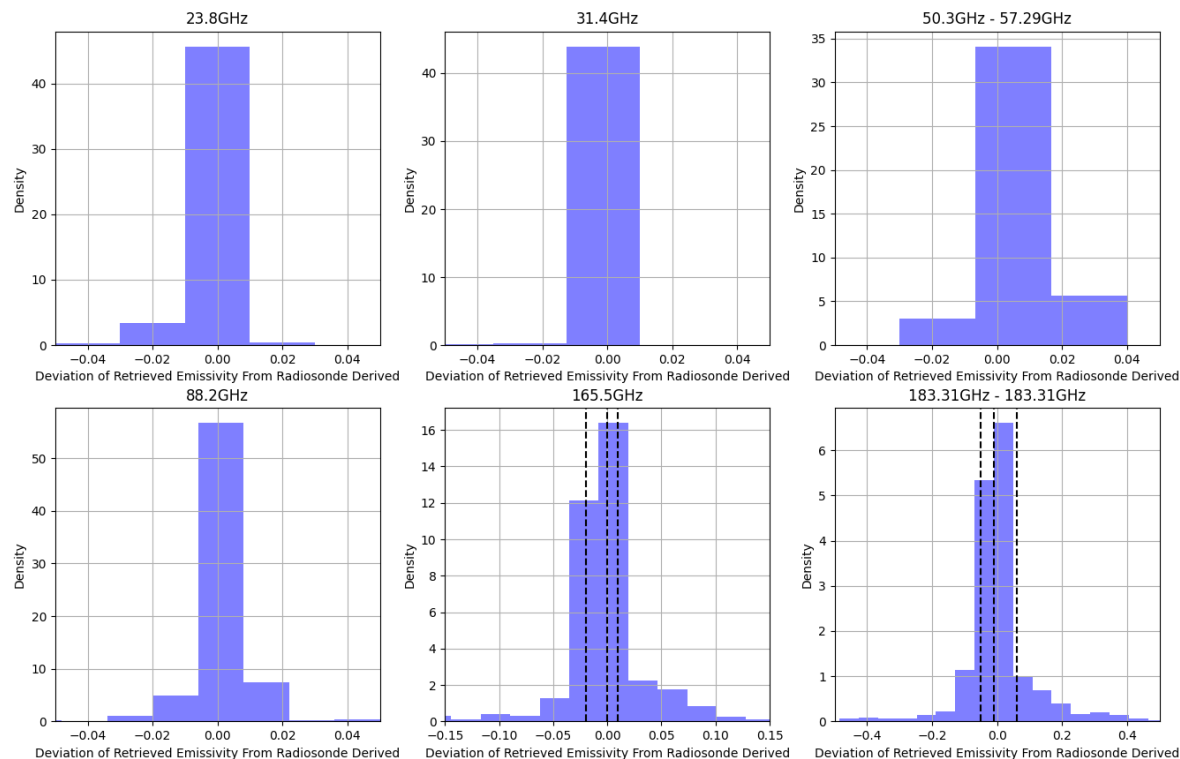
Figure 8 Histogram of the surface emissivity retrieved in our study compared to the radiosonde reference value. The dashed black lines represented the median value and the 68% confidence intervals (one standard deviation) in the lower middle and lower right panels.

The changes in surface emissivity over the year provide information about melting events in the ice sheet. Figure 9 presents surface emissivity from November 2015 to the end of 2016 at three window frequencies and near the oxygen absorption band. The blue curve represents values obtained from our iterative algorithm, while the red dashed line shows the radiosonde reference values. These values are in good agreement with each other. Two melting events were observed around mid-December 2015 and mid-January 2016, as indicated by the black arrows. The melting event in mid-January was more significant. Following the melting event, the emissivity decreased due to ice crust formation within the surface snow during the refreezing, which increases scattering and depresses brightness temperature, resulting in reduced effective emissivity. Figure 10 displays temperature and specific humidity perturbations from January to March 2016, covering the period of the melting events and the availability of radiosonde measurements. These perturbations show deviations of the profiles from the average values during the specified period (from 2016.01.01 to 2016.03.31). The top row shows results from our iterative algorithm, while the bottom row shows profiles measured using radiosonde. Despite the higher vertical resolution in radiosonde measurements, our iterative algorithm captures the temperature and humidity variations effectively. The melting events in mid-January corresponded with increases in near-surface temperature and humidity, as indicated by the black arrows. Temperature increased by over 10 K during the melting event.
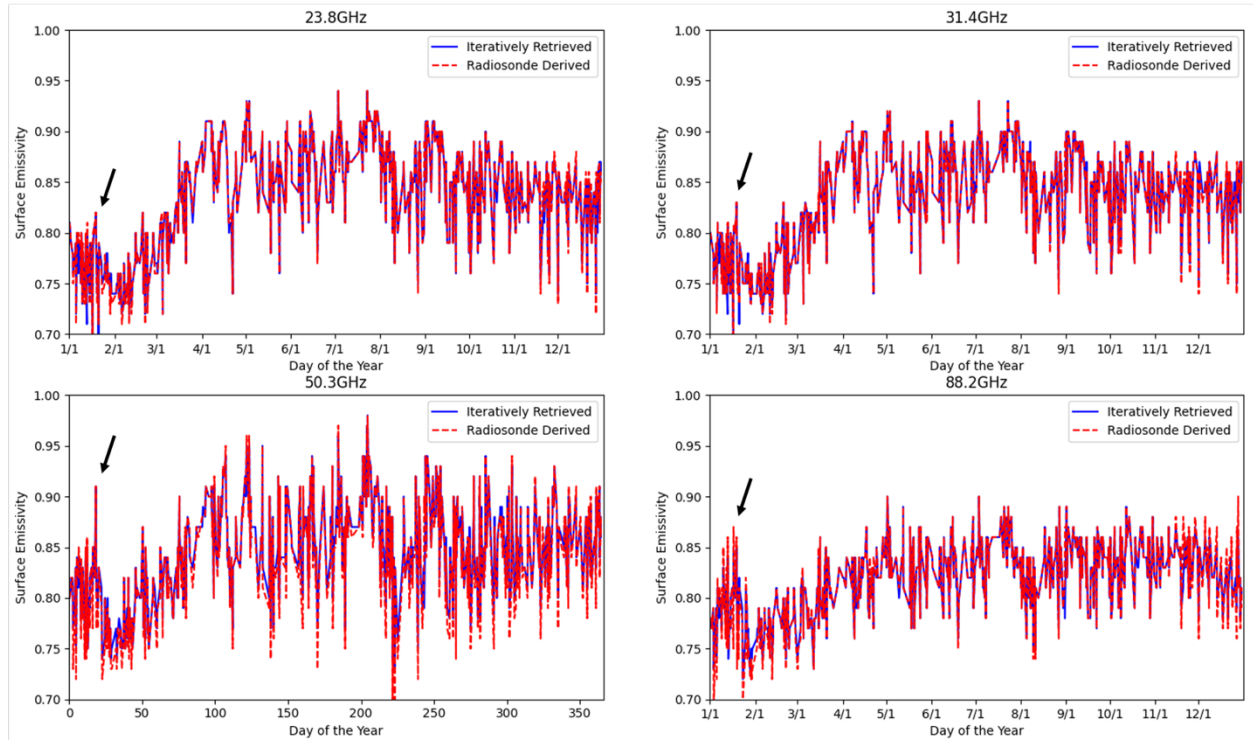
Figure 9 McMurdo Radiosonde Station (77.85ºS, 166.66ºE). Surface emissivity from November 2015 to the end of 2016 at three window frequencies (23.8GHz, 31.4GHz and 88.2GHz) and the oxygen absorption band (50GHz – 58GHz). The blue curve represents values from our iterative algorithm and the red dashed line shows values derived from the radiosonde measurements. Two melting events occurred in mid-December and mid-January, pointed out by the black arrows. The X-axis shows the month of the year, from 2015/11/1 to 2016/12/31.

345
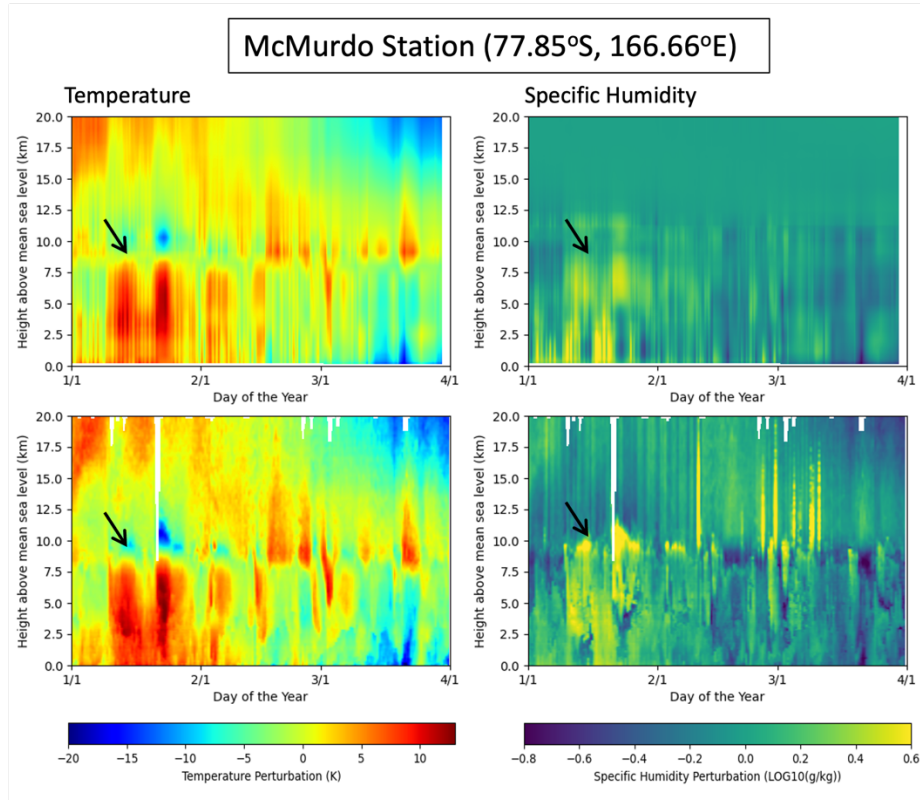
346 **Figure 10** McMurdo Radiosonde Station (77.85ºS, 166.66ºE). Temperature and specific humidity perturbations

347 during January to March 2016. The deviations from average values are displayed for that period. The top row presents

348 results from our iterative algorithm, while the bottom row shows data from radiosonde measurements. Melting events

349 in mid-January correspond to the temperature and humidity increases around the same time. The X-axis shows the

350 month of the year, from 2016/01/01 to 2016/03/31. The temporal resolution in the map is based on an interpolation of

351 ATMS observed data time intervals, which are approximately a few hours apart.

352

353 **WAIS Divide Station**

354

355 The WAIS Divide Station is located at coordinates 79.468ºS, 112.086ºW, with an altitude of approximately 1.8 km

356 above sea level. Detailed radiosonde measurements were taken between January 1st and January 15th, 2016. Figure

357 11 compares the temporal fluctuations of temperature and specific humidity throughout January, along with surface

358 emissivity (bottom panel), between the iterative retrievals (top row) and radiosonde measurements (middle row). By

359 utilizing the iterative retrieval method, we were able to accurately track the rise in temperature and humidity from

360 January 10th to January 15th, aligning with the melting of the Ross Ice shelf as recorded at McMurdo Station in mid-

361 January. In contrast to the surface emissivity changes observed at McMurdo Station, no substantial variations in

362 surface emissivity were noted at the WAIS Divide Station, indicating stable ice crust structures and limited snowfall

363 during the summer months. Although near surface temperatures increased, they did not reach levels sufficient to

364 initiate melting at this inland location.

365
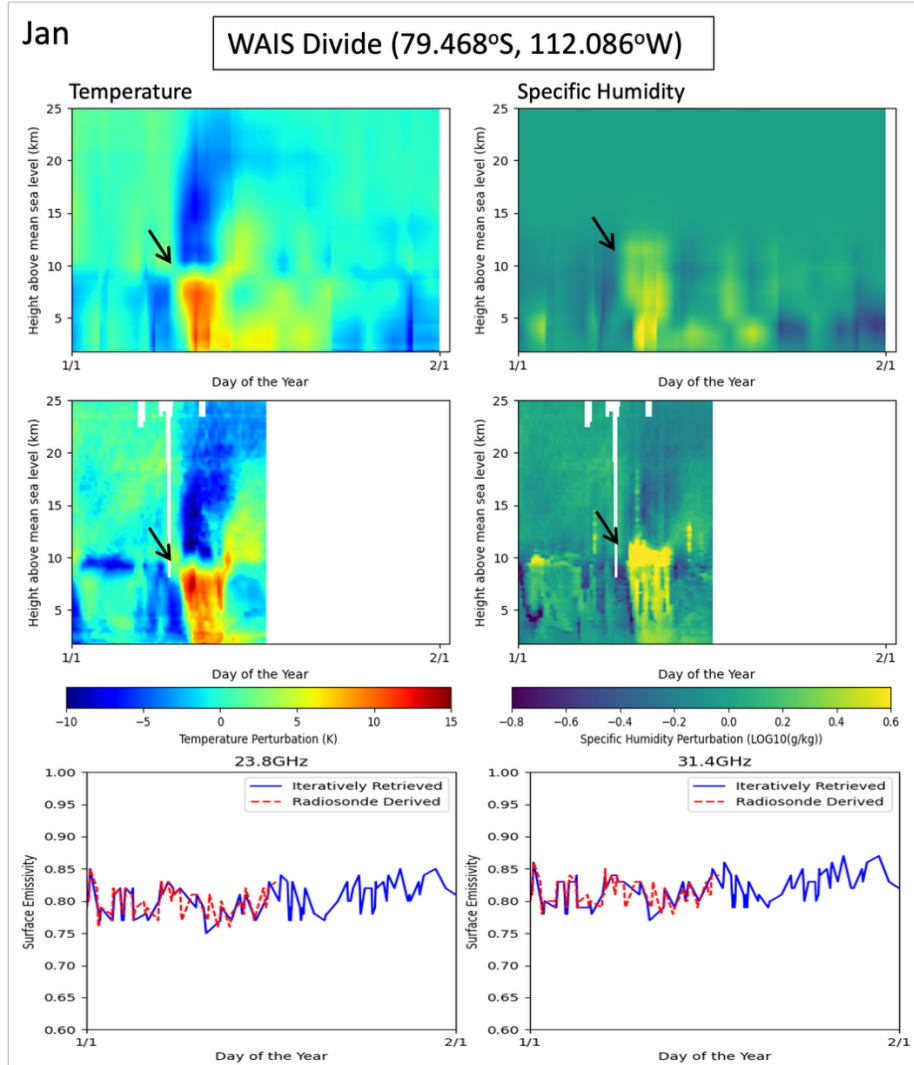
Figure 11 WAIS Divide Radiosonde Station (79.468°S, 112.086°W). Temperature and specific humidity perturbations during January 2016. The deviations from average values are displayed for that period. The top row presents results from our iterative algorithm, while the middle row shows data from radiosonde measurements. The X-axis shows the month of the year, from 2016/1/1 to 2016/1/31. Bottom panels: Surface emissivity at two window frequencies (23.8GHz, 31.4GHz). The blue curve represents values from our iterative algorithm and the red dashed line shows values derived from the radiosonde measurements.

Ross Ice Shelf

In January 2016, a significant surface melting event was documented that impacted a significant section of the Ross Ice Shelf (Nicolas et al., 2017; Mousavi et al., 2022; de Roda Husman et al., 2024; Hansen et al., 2024). The melting is associated with the strong and continuous transport of warm marine air to the region, likely influenced by the concurrent powerful El Nino event. The broad atmospheric fluctuations during and following the melting incident are

381 found to be established by the El Nino event and mitigated by the positive Southern Annular Mode. These atmospheric
382 changes are identified by our iterative method, as illustrated in Fig. 10 and Fig. 11. We present findings at the
383 coordinates 83ºS, 153ºW at the center of the melting incident. As indicated in Figure. 12, there is a sharp rise in surface
384 emissivity from 23.8 to 58 GHz, indicating surface melting over ice sheets and the presence of liquid water in the
385 snowpack. Our iterative analysis of temperature and humidity perturbations captures the significant and vertically
386 extensive intrusion of marine air from 10-13 January.

387
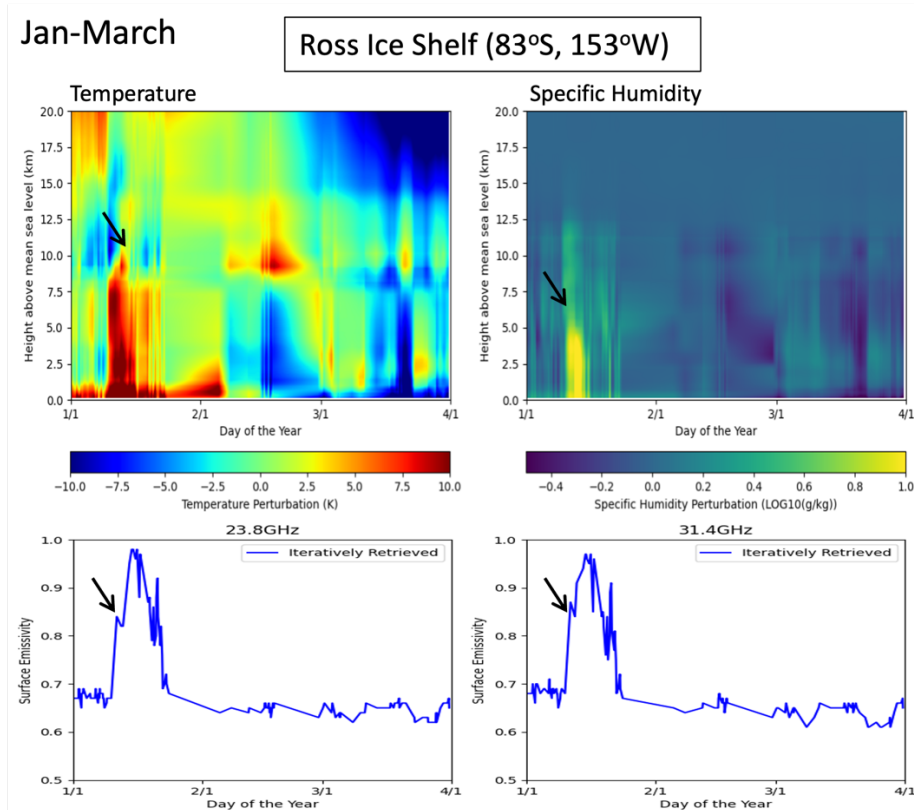
388 **Figure 12** Ross Ice Shelf (83ºS, 153ºW). Temperature and specific humidity perturbations during January 2016 to
389 March 2016. The deviations from average values are displayed for that period. The results are retrieved using our
390 iterative algorithm. The X-axis shows the month of the year, from 2016/1/1 to 2016/3/31. Bottom panel: Surface
391 emissivity at window frequencies (23.8, 31.4). The blue curve represents values from our iterative algorithm. The
392 melting events occurred in mid-January, pointed out by the black arrows.

393

394 **4.2 West & East Coast Ice Shelves During 2016**

395

396 In the Antarctica region, ice shelves cover approximately 1.5 million square kilometers and include major formations
397 such as the Ross , Ronne-Filchner , and Larsen Ice Shelf. Ice shelf melt can lead to an accelerated ice discharge from
398 the land into the ocean, significantly contributing to the global sea level rise. Melting events over these ice shelves
399 are, therefore, critical to understanding and predicting future sea level changes.

400

401 The west coast of Antarctica is home to several ice shelves, including the Larsen C , Wilkins , and George VI Ice
402 Shelf, all situated on the Antarctic Peninsula. These ice shelves exhibit similar annual variations in surface properties.
403 Notably, multiple surface emissivity increases are observed throughout the year (Figure 13, upper left panel). labeled
404 as events 1 through 8. Figure 14 presents the temperature and humidity perturbations associated with these surface
405 emissivity changes, with each event number indicated. These emissivity changes are generally correlated with
406 increases in atmosphere temperature and humidity, though they likely arise from a range of underlying causes.. Figure
407 13 upper middle panel displays the skin temperature data from ERA5 [Hersbach et al., 2023], with the black dashed
408 line representing the melting point at 273K. During the summer months (January to March and November to
409 December), increased emissivity corresponds to elevated skin temperatures reaching the melting threshold. An
410 additional melting event detected in early May (event 4) is attributed to concurrent rises in both near-surface
411 atmospheric temperature and skin temperature. Conversely, the increased emissivity observed in late May (event 5)
412 is attributed to rainfall. These findings underscore the complex interplay of climatic factors driving the surface
413 emissivity change on the Antarctic Peninsula's ice shelves, highlighting the sensitivity of these regions to both
414 temperature and precipitation changes.

415

416 On the other hand, East coast ice shelves, such as the Amery and Shackleton Ice Shelf, exhibit very difference yearly
417 variations in surface conditions. Unlike the complex interactions observed around the west coast, potential melting
418 events on the east coast—indicated by increases in surface emissivity as shown in Fig. 13 (lower left)—are detected
419 exclusively during the summer months of January and December. According to ERA5 data (Fig. 13, lower middle and
420 right), the east coast experiences extremely dry conditions with nearly no precipitation of rain. These melting events
421 are attributed solely to the increase in near-surface atmospheric temperature and skin temperature, which rise above
422 the melting point during the summer.

423
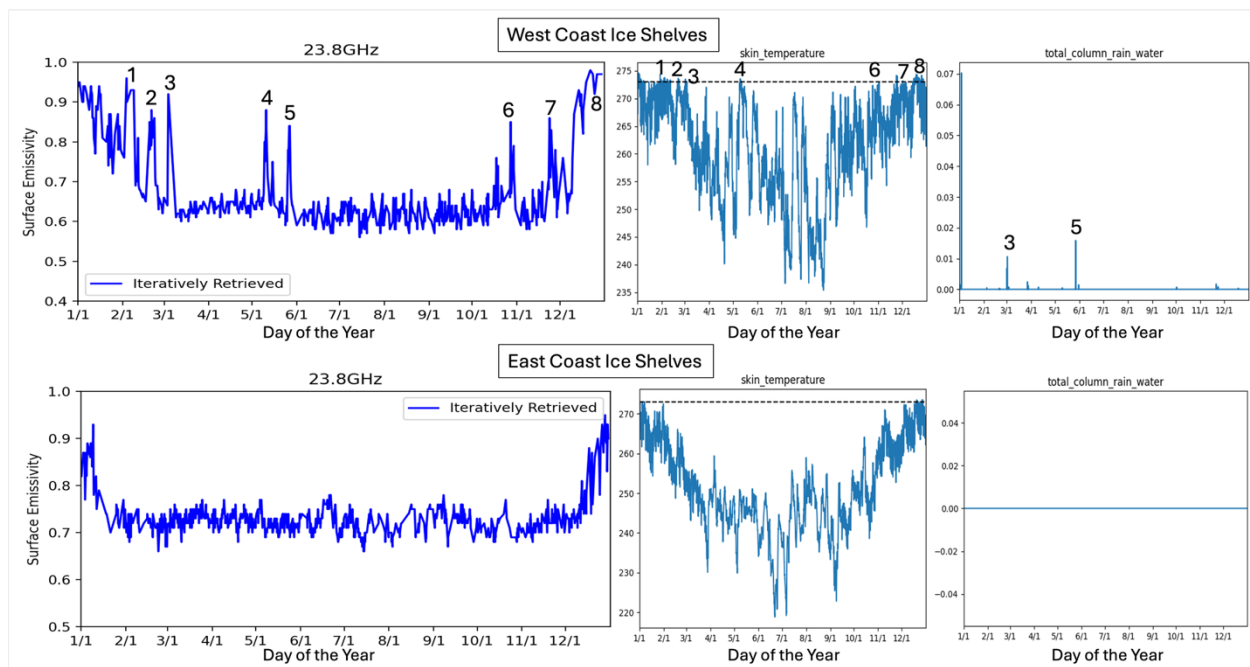
Figure 13 Upper row: West coast - Larsen C Ice Shelf (67.5ºS, 62.5ºW). Surface emissivity variation at 23.8GHz (left) shows a few significant increases during summer months and May. The results are retrieved using our iterative algorithm. A few emissivity increases are observed (labeled 1 through 8). Skin temperature (middle) and precipitation of rain (right) from ERA5 are presented. The X-axis shows the month of the year, from 2016/1/1 to 2016/12/31. Lower row: East coast - Amery Ice Shelf (70ºS, 71ºE). Surface emissivity variation at 23.8 GHz (left) shows potential melting events only during the summer months.
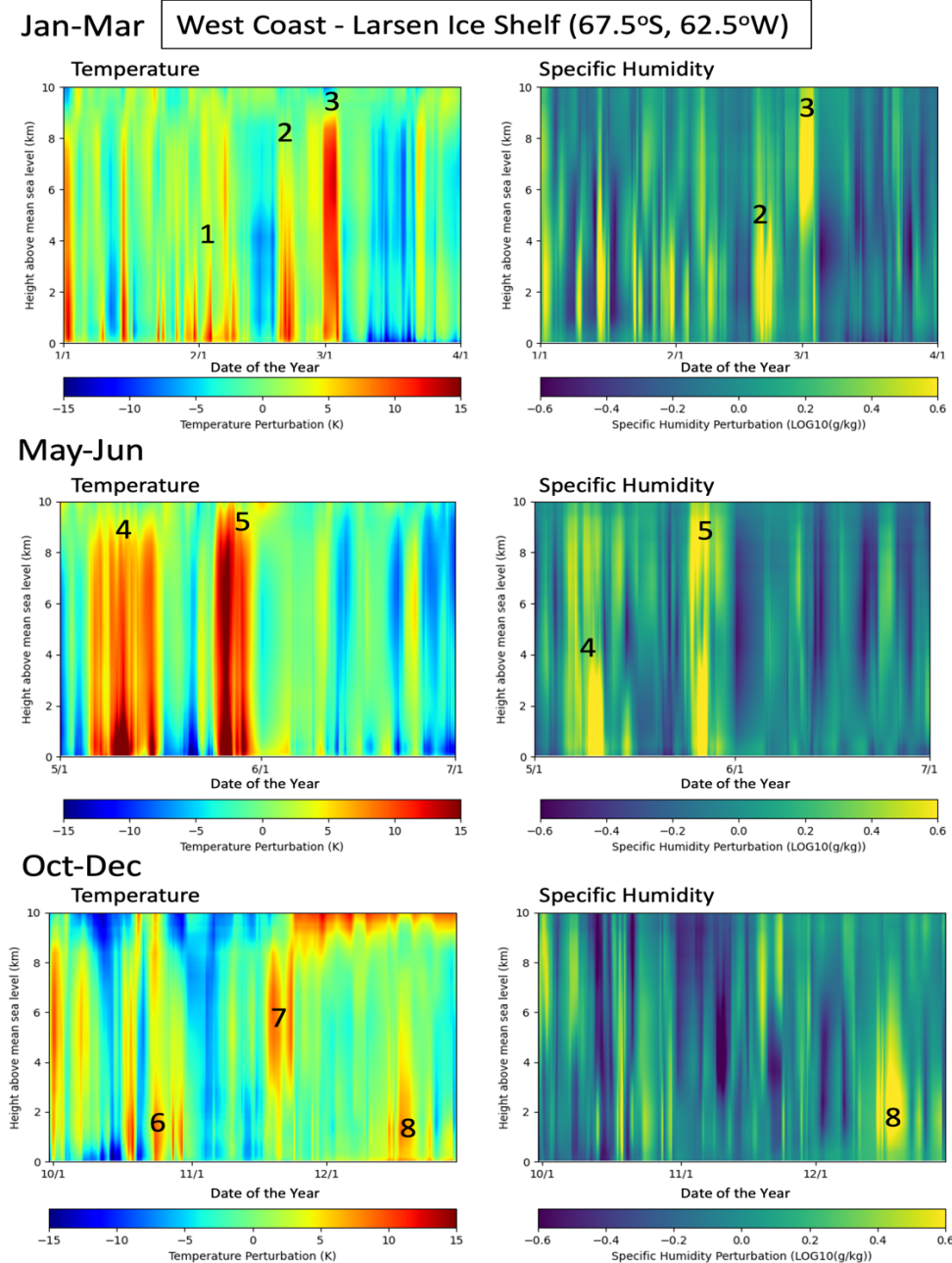
Figure 14 Larsen C Ice Shelf (67.5ºS, 62.5ºW). The corresponding temperature/humidity perturbations during the emissivity increase events—first labeled in Fig. 13—are shown here and indicated using the same event numbers.

434

435

5   Conclusion

437

This study presents a novel iterative retrieval algorithm that couples atmospheric profile retrieval with surface emissivity estimation, applied to ATMS observations across Antarctica. This coupled approach enables improved retrieval of atmospheric states in the challenging conditions of polar environments where surface emission is complex and temporally variable due to melting and refreezing events. Validation against high-resolution radiosonde measurements from multiple Antarctic stations in 2016 demonstrates the algorithm's capability in retrieving atmospheric temperature profiles, with a typical retrieval accuracy of ±0.5 K. Surface emissivity estimates at transparent window and oxygen absorption channels (i.e., 23.8 - 88.2 GHz) are accurate within ±0.01–0.02. However, atmospheric humidity retrieval accuracy diminishes at higher frequencies, especially near the 183 GHz water vapor absorption band, where emissivity is entangled with near-surface humidity contributions. Water vapor retrievals, though able to resolve temporal variability, showed an absolute uncertainty up to 25%, indicating that reliable retrieval of humidity requires independent emissivity estimates at water vapor-sensitive frequencies.

449

The study also reveals significant spatial variability across Antarctic regions. The Ross Ice Shelf exhibited pronounced emissivity and atmospheric changes during the 2016 mid-January melting event, aligning with observed marine air intrusions. In contrast, locations such as the WAIS Divide showed minimal emissivity variation despite similar atmospheric warming. West Antarctic coastal ice shelves (e.g., Larsen) exhibit complex emissivity variations throughout the year, influenced by both temperature fluctuations and precipitation events, whereas East Antarctic shelves (e.g., Amery) maintain more stable surface emissivity characteristics.

456

Future improvement hinges on integrating this retrieval framework with independent multi-frequency algorithms for estimating ice sheet surface properties (e.g., meltwater fraction, snow density), which can decouple surface and atmospheric signals. Such hybrid retrieval schemes are vital for robust long-term monitoring of polar climate feedbacks and for improving the accuracy of model-based predictions of how ice sheets will respond to future atmospheric conditions.

Data/Code Availability

The data used in this study is publicly available:

1. ATMS: Weng, Fuzhong, Sun, Ninghai, Qiu, Shuang, and NOAA JPSS Program Office (2011): NOAA JPSS Advanced Technology Microwave Sounder (ATMS) Sensor Data Record (SDR) from IDPS. [ATMS brightness temperature over Antarctic region (<60°S), channels 1–22, January-December 2016]. NOAA National Centers for Environmental Information. doi:10.7289/V5BR8Q7N [Accessed 2023.01].

https://www.class.noaa.gov/saa/products/search?datatype_family=ATMS_SDR

469   2. MERRA2: Global Modeling and Assimilation Office (GMAO) (2015), MERRA-2 tavg3_3d_asm_Nv: 3d, 3-

470   Hourly, Time-Averaged, Model-Level, Assimilation, Assimilated Meteorological Fields V5.12.4,

471   10.5067/SUOQESM06LPK; tavg1_2d_slv_Nx: 2d, 1-Hourly, Time-Averaged, Single-Level, Assimilation, Single-

472   Level Diagnostics V5.12.4, 10.5067/VJAFPLI1CSIV, Greenbelt, MD, USA, Goddard Earth Sciences Data and

473   Information Services Center (GES DISC), Accessed 2023.01. https://disc.gsfc.nasa.gov/

474   The retrieval code is publicly available at: https://github.com/zz246/AtmoIterativeSolver

Competing Interests

The contact author has declared that none of the authors has any competing interests.

Author Contribution

Zhimeng Zhang developed the algorithm, conducted the analyses, and wrote the manuscript. Andreas Colliander originated the algorithm concept, supervised the analysis, and contributed to manuscript review and editing. Shannon Brown provided oversight for the analytical work.

Acknowledgements

This work is funded by the NASA Cryosphere Program. A contribution to this work was made at the Jet Propulsion Laboratory, California Institute of Technology, under a contract with National Aeronautics and Space Administration.

6   References

[1] Imke Durre, Russell S. Vose, and David B. Wuertz. (2006) "Overview of the Integrated Global Radiosonde Archive". Journal of climate. DOI: 10.1175/JCLI3594.1

[2] Goldberg, M.D., Weng, F. (2006). "Advanced Technology Microwave Sounder". In: Qu, J.J., Gao, W., Kafatos, M., Murphy, R.E., Salomonson, V.V. (eds) Earth Science Satellite Remote Sensing. Springer, Berlin, Heidelberg. https://doi.org/10.1007/978-3-540-37293-6_13

[3] Hansen, N., Orr, A., Zou, X., Boberg, F., Bracegirdle, T. J., Gilbert, E., Langen, P. L., Lazzara, M. A., Mottram, R., Phillips, T., Price, R., Simonsen, S. B., and Webster, S.: The importance of cloud properties when assessing surface melting in an offline-coupled firn model over Ross Ice shelf, West Antarctica, The Cryosphere, 18, 2897–2916, https://doi.org/10.5194/tc-18-2897-2024, 2024.

[4] Hersbach, H., Bell, B., Berrisford, P., Biavati, G., Horányi, A., Muñoz Sabater, J., Nicolas, J., Peubey, C., Radu, R., Rozum, I., Schepers, D., Simmons, A., Soci, C., Dee, D., Thépaut, J-N. (2023): ERA5 hourly data on single levels from 1940 to present. Copernicus Climate Change Service (C3S) Climate Data Store (CDS), DOI: 10.24381/cds.adbb2d47 (Accessed on DD-MMM-YYYY)

[5] Sophie de Roda Husman, Stef Lhermitte, Jordi Bolibar, Maaike Izeboud, Zhongyang Hu, Shashwat Shukla, Marijn van der Meer, David Long, Bert Wouters, A high-resolution record of surface melt on Antarctic ice shelves using multi-source remote sensing data and deep learning, Remote Sensing of Environment, Volume 301, 2024, 113950, ISSN 0034-4257, https://doi.org/10.1016/j.rse.2023.113950.

[6] Kim, E.; Lyu, C.-H. J.; Anderson, K.; Leslie, R. V.; Blackwell, W. J. (2014), "S-NPP ATMS instrument prelaunch and on-orbit performance evaluation", J. Geophys. Res. Atmos., 119 (9): 5653–5670, Bibcode:2014JGRD..119.5653K, doi:10.1002/2013JD020483, hdl:2060/20140017425

[7] Kim, E.; et al. (2020). "Pre-launch performance of the Advanced Technology Microwave Sounder (ATMS) on the Joint Polar Satellite System-2 Satellite (JPSS-2)". International Geoscience and Remote Sensing Symposium. Waikoloa, HI, USA. pp. 6353–6. doi:10.1109/IGARSS39084.2020.9324605.

[8] Lubin, Daniel, Bromwich, David H, Vogelmann, Andrew M, Verlinde, Johannes, and Russell, Lynn M. ARM West Antarctic Radiation Experiment (AWARE) Field Campaign Report. United States: N. p., 2017. Web.

[9] M. L. Meeks, A. E. Lilley. (1963) "The microwave spectrum of oxygen in the Earth's atmosphere". JGR Volume68, Issue6. DOI: 10.1029/JZ068i006p01683

[10] Miao J., K. Kunzi, G. Heygster. (2001). "Atmospheric Water Vapor over Antarctica Derived from Special Sensor Microwave/Temperature 2 Data". J. Geophy. Research, Vol. 106, No. D10, pp. 10,187-10,203. Mote, T.L., and M.R. Anderson

[11] M. Mousavi, A. Colliander, J. Z. Miller and J. S. Kimball, "A Novel Approach to Map the Intensity of Surface Melting on the Antarctica Ice Sheet Using SMAP L-Band Microwave Radiometry," in *IEEE Journal of Selected Topics in Applied Earth Observations and Remote Sensing*, vol. 15, pp. 1724-1743, 2022, doi: 10.1109/JSTARS.2022.3147430.

[12] C. Muth, W. A. Webb, W. Atwood and P. Lee, "Advanced technology microwave sounder on the National Polar-Orbiting Operational Environmental Satellite System," Proceedings. 2005 IEEE International Geoscience and Remote Sensing Symposium, 2005. IGARSS '05., Seoul, Korea (South), 2005, pp. 4 pp.-, doi: 10.1109/IGARSS.2005.1526113.

[13] T. L. Noble, E. J. Rohling, A. R. A. Aitken, H. C. Bostock, Z. Chase, N. Gomez, L. M. Jong, M. A. King, A. N. Mackintosh, F. S. McCormack, R. M. McKay, L. Menviel, S. J. Phipps, M. E. Weber, C. J. Fogwill, B. Gayen, N. R. Golledge, D. E. Gwyther, A. McC. Hogg, Y. M. Martos, B. Pena-Molino, J. Roberts, T. van de Flierdt, T. Williams. (2020) "The Sensitivity of the Antarctic Ice Sheet to a Changing Climate: Past, Present, and Future". Volume58, Issue4, The Global Climate Crisis: From Research to Solutions. DOI: 10.1029/2019RG000663.

[14] Grant W. Petty. (2023) "A First Course in Atmospheric Radiation". Sundog Publishing LLC.

[15] Rosenkranz, P. W. (2001). Retrieval of temperature and moisture profiles from AMSU-A and AMSU-B measurements. IEEE Transactions on Geoscience and Remote Sensing, vol. 39, no. 11, pp. 2429-2435. doi: 10.1109/36.964979.

[16] E. Rignot, I. Velicogna, M. R. van den Broeke, A. Monaghan, J. T. M. Lenaerts. (2011) "Acceleration of the contribution of the Greenland and Antarctic ice sheets to sea level rise". Volume38, Issue5, GRL 40th Anniversary Special Collection. DOI: 10.1029/2011GL046583.

[17] Roger Saunders, James Hocking, Emma Turner, Peter Rayer, David Rundle, Pascal Brunel, Jerome Vidot,Pascale Roquet, Marco Matricardi, Alan Geer, Niels Bormann, and Cristina Lupu. (2018) "An update on the RTTOV fast radiative transfer model (currently at version 12)". Volume 11, issue 7, EGU. https://doi.org/10.5194/gmd-11-2717-2018

541 [18] Sébastien Le clec'h, Sylvie Charbit, Aurélien Quiquet, Xavier Fettweis, Christophe Dumas, Masa

542 Kageyama,Coraline Wyard, and Catherine Ritz. (2019) "Assessment of the Greenland ice sheet–atmosphere

543 feedbacks for the next century with a regional atmospheric model coupled to an ice sheet model". European

544 Geosciences Union. DOI: 10.5194/tc-13-373-2019.

545 [19] Spencer, Roy W and William D Braswell.1999. ADVANCED MICROWAVE SOUNDING UNIT-A (AMSU-

546 A) SWATH FROM NOAA-15. Dataset available online from the NASA Global Hydrometeorology Resource Center

547 DAAC, Huntsville, Alabama, U.S.A. DOI: http://dx.doi.org/10.5067/GHRC/AMSU-A/DATA201

548 [20] Xu, M.; Li, Y.; Yang, Q.; Gao, A.E.; Han, B.; Yang, Y.; Yu, L.; Wang, L. Radiosonde-Observed Vertical Profiles

549 and Increasing Trends of Temperature and Humidity during 2005–2018 at the South Pole. Atmosphere 2019, 10, 365.

550 https://doi.org/10.3390/atmos10070365

551 [21] Global Modeling and Assimilation Office (GMAO) (2015), MERRA-2 tavg3_3d_asm_Nv: 3d,3-Hourly,Time-

552 Averaged,Model-Level,Assimilation,Assimilated Meteorological Fields V5.12.4, Greenbelt, MD, USA, Goddard

553 Earth Sciences Data and Information Services Center (GES DISC), 10.5067/SUOQESM06LPK

554 [22] Global Modeling and Assimilation Office (GMAO) (2015), MERRA-2 tavg1_2d_slv_Nx: 2d,1-Hourly, Time-

555 Averaged,Single-Level,Assimilation,Single-Level Diagnostics V5.12.4, Greenbelt, MD, USA, Goddard Earth

556 Sciences Data and Information Services Center (GES DISC), 10.5067/VJAFPLI1CSIV

557 [23] Ferraro, Ralph R.; Meng, Huan; Yang, Wenze; and NOAA CDR Program (2016). NOAA Climate Data Record

558 (CDR) of Advanced Microwave Sounding Unit (AMSU)-A, Version 1.0. NOAA National Centers for Environmental

559 Information. doi:10.7289/V53R0QXD.

560 [24] Rienecker, M. M., and Coauthors, 2008: The GEOS-5 Data Assimilation System—Documentation of versions

561 5.0.1 and 5.1.0, and 5.2.0. NASA Tech. Rep. Series on Global Modeling and Data Assimilation, NASA/TM-2008-

562 104606, Vol. 27, 92 pp.

563 [25] Ferraro, R.R., Nelson, B.R., Smith, T. and Prat, O.P., 2018. The AMSU-based hydrological bundle climate data

564 record—Description and comparison with other data sets. Remote Sensing, 10(10), p.1640.

565

566

567

568